Gaussian beam shaping and multivariate analysis in plasmonic sensing

Jaione Etxebarria-Elezgarai [1,*], Miriam Mowat [1], Eneko Lopez [1], Carlos Rodríguez [1], Ion Olaetxea [1], Andreas Seifert [1,2,*]

[1]CIC nanoGUNE BRTA, Tolosa Hiribidea 76, 20018 Donostia - San Sebastián, Spain

[2]IKERBASQUE, Basque Foundation for Science, Euskadi Plaza 5, 48009 Bilbao, Spain

Authors information:

J. E. E.*: j.etxebarria@nanogune.eu; tel: +34 943 57 40 66,

M. M.: miriamlm@hotmail.co.uk,

E. L. C.: e.lopez@nanogune.eu,

C. R. M.: carlos_rdz96@hotmail.com,

I. O. A.-A.: i.olaetxea@nanogune.eu,

A.S.*: a.seifert@nanogune.eu; tel: +34 943 57 40 45

Abstract

This work demonstrates a novel strategy to improve the sensing performance of a prism-coupled surface plasmon resonance system by Gaussian beam shaping and multivariate data analysis. The propagation of the beam along the optical system has been studied using the Gaussian beam approximation to design the incident beam such that the beam waist is aligned precisely, and that stability is assured at the metal-dielectric interface. This renders a collimated incident beam, hence least angular dispersion, yielding a stronger and sharper plasmonic resonance. Moreover, we use the multivariate analysis method Partial Least Squares that combines multiple features of the surface plasmon resonance curve and allows for a more precise analysis of the plasmonic response. Compared to univariate analysis, partial least squares improves typical sensing performance parameters remarkably. The combination of both aspects, beam shaping and multivariate analysis, overcomes current limitations of plasmonic detection systems. Thereby, we improve analytical sensitivity by a factor of 16; decrease the prediction error of the concentration of an unknown analyte by a factor of 11; and enhance resolution to the order of 5×10^{-7} RIU in angular interrogation.

INTRODUCTION

Surface plasmon resonance (SPR) systems represent highly sensitive bioanalysis techniques for label-free detection of molecules in real-time [1, 2]. The working principle is based on light-metal interaction at metal-dielectric interfaces that creates charge density oscillations called surface plasmon polaritons (SPPs). These SPPs are highly sensitive to refractive index (RI) changes close to the sensing surface [3]. The most frequent configuration in SPR systems is the *Kretschmann* configuration, Figure 1a. It employs a coupling-prism to fulfill the resonance condition, causing a sharp decrease in the reflected beam intensity, as shown in Figure 1b., which is highly sensitive with respect to the RI of the surrounding medium. Thereby, any change in the RI due to the sample at close proximity to the metal surface induces a detectable change in the behavior of the reflected light, associated with plasmon-related features (angle, wavelength, phase) [4, 5]. In commercial biosensors a single parameter is usually monitored in the SPR sensograms, for example the incident angle at minimum reflectance as a function of time. However, some examples of multi-parametric surface plasmon resonance detection have been reported, for instance with the goal of characterizing biomolecular layers in more detail for determination of layer thicknesses, refractive indices and surface mass densities in addition to traditional binding kinetics analysis [6]. In this case, several parameters were monitored in real-time, such as the angle for total internal reflection, the angular position of the resonance condition, the half-width of the SPR peak and the change in the main SPR peak intensity at resonance. Similarly, the commercial BioNavis instruments employ multi-parametric SPR to provide a technology that features a single measurement channel, thus eliminating the need for any reference channel. As a result, clean

sensograms without bulk artifacts can be obtained, and nanolayer thicknesses, refractive indices and nanoparticle properties can be measured.
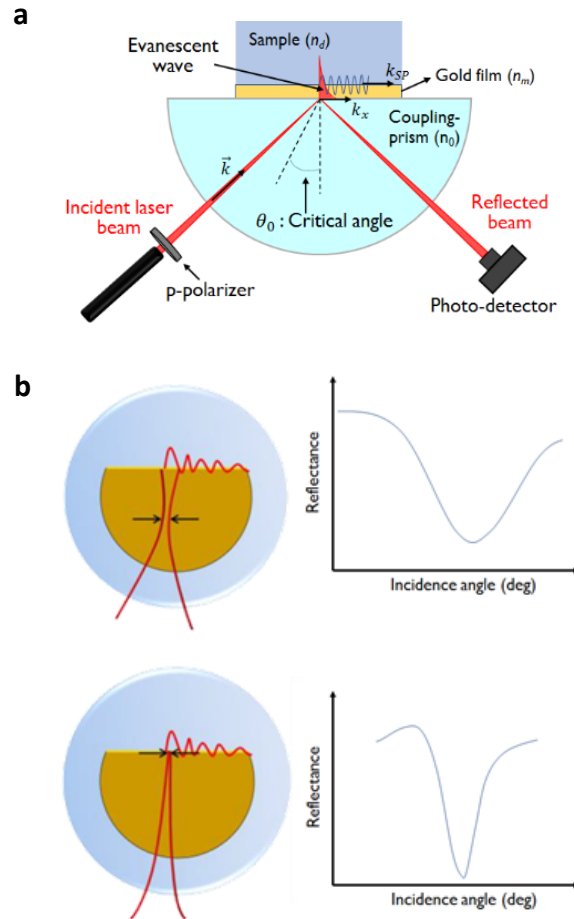

Figure 1: Schematic representation of the working principle of an SPR system. (a) SPR system in Kretschmann configuration with cylindrical prism. (b) Involvement of the incident beam profile in the plasmonic response of a Kretschmann configuration with angular interrogation. An incident beam that is not aligned (shaped) and shows angular dispersion at the metal-dielectric interface, yields broader plasmonic resonance and decreased resonance strength.

Many sensing applications call for enhanced sensitivity, better resolution, and lower detection limits. For instance, big efforts have been put into nanoscale engineered metasurfaces [7-9], leading to real-time and label-free nanoplasmonic biosensors for point-

of-care device development [10-13]. Other approaches propose the use of 2D materials to enhance the sensitivity of the plasmonic metasurfaces [14-16]. In the case of purely propagating plasmons at flat metal surfaces, the sensitivity cannot be enhanced beyond a certain limit, due to the limitations imposed by light-matter interactions. Generally, when designing an SPR system, a plane incident wave is assumed [17, 18]. In practice, even highly collimated laser sources have a propagating laser beam that occurs in the form of a Gaussian beam and present angular dispersion, which strongly depends on the characteristics of the light source used [19]. Moreover, in SPR systems the incident beam is usually focused to a very small spot to increase the electric field intensity and improve signal-to-noise ratio [20]. Consequently, a short Rayleigh range of the Gaussian beam is achieved and it is technically very difficult to place the beam waist directly at the interface, resulting in a dispersion of incident angles. Unlike the response of an ideal plane wave, the plasmonic resonance becomes broader and shows decreased resonance strength, which diminishes the resolution of the measurement [20], as schematically shown in Figure 1b. Gaussian beam shaping can be done by simple refractive components or by more sophisticated methods to achieve the requirements for the wave characteristics defined by the experiment or application [21].

The profile and the propagation of the beam through an optical system can be described by the Gaussian beam approximation [22, 23] by

$$\frac{1}{q} = \frac{1}{R(z)} - i \frac{\lambda}{\pi W^2(z)} \ , \qquad\qquad (1)$$

where q is a complex parameter that combines the position and width of the beam, z is the propagation axis, λ the wavelength, and $R(z)$ and $W(z)$ are the radius of curvature and the half width of the beam at position z, respectively. $W(z)$ is expressed by

$$W(z) = w_0\sqrt{1 + \left(\frac{\lambda(z-d_0)}{\pi w_0{}^2}\right)^2}, \qquad (2)$$

with w_0 being the half width of the beam at the beam waist, at position $z = d_0$.

In this context, this work demonstrates the optimization of the plasmonic response by shaping and placing the beam waist exactly at the metal-dielectric interface, which is expected to provide stronger plasmonic performance. The design of the optical system is analytically calculated, and numerically optimized, using Gaussian ray tracing. Thereby, the Gaussian beam approximation model is resolved for a customized SPR system built in Kretschmann configuration, where the position and the refractive power of all beam shaping components is considered. In addition, analytical calculations are complemented by optical ray tracing using OpticStudio®-Professional-SUL from Zemax. The optimum solution is experimentally verified in the customized SPR system, featuring a semi-cylindrical prism and a beam shaping lens. This optimized configuration is validated by the performance of the SPR system via univariate analysis (UVA) for RI changes using sucrose solutions as analyte at different concentrations. The same characterization procedure is carried out for the SPR system without the beam shaping to determine the enhancement in SPR performance due to Gaussian beam shaping. Additionally, instead of conventional univariate methods that solely measure the shift of the resonance angle, multivariate data processing is employed to further analyze the results obtained for both

systems, with and without beam shaping. Multivariate analysis (MVA) collects more information from the SPR curve by combining multiple characteristic features, resulting in more precise analysis and better performance in terms of analytical sensitivity and prediction errors.

MATERIAL AND METHODS

SPR biosensing system and measurements

A customized SPR system is built in Kretschmann configuration using a semi-cylindrical coupling-prism for angle interrogation, as shown in Figure S7a [24]. The system consists of a p-polarized monochromatic He-Ne laser source (λ = 632.8 nm, HRS015B, Thorlabs, USA), a Faraday rotator (IO-2D-633-VLP, Thorlabs), a beam shaping refractive component (LB 1904 bi-convex lens, Thorlabs), a beam splitter for a reference signal and SPR detector (CCM1-BS013/M, Thorlabs), and a semi-cylindrical coupling-prism (Schott N-SF57, n_{SF57} = 1.8395 at λ = 633 nm, Crysmit Photonics, China) that is housed on a rotating platform (M-060.DG DC, PI miCos, Spain). The rotating platform is mounted together with a prism-holder to ensure a completely centered and reproducible placing of the coupling-prism. Additionally, a second rotating platform (OSMS-60YAW, OptoSigma, France) is used for the photodetector (PDA100A-EC, Thorlabs) to allow independent motion of the prism and the detector. The two rotating platforms are built on three linear translational stages (PLS-85, Pi miCos), which allows for alignment of the coupling-prism with the optical path and especially for fine-tuning the distance between the beam shaping lens and the coupling-prism.

A special holder is fabricated by 3D printing (see Figure S5) to attach a plasmonic device on the customized SPR system. The plasmonic biosensor is fabricated by direct physical vapor deposition of 50 nm thin film of Au on top of a 170 µm BK7 glass substrate. Prior to the deposition process, the BK7 substrate is cleaned in an ultrasonic bath using Acetone and Isopropanol as solvents, 5 minutes each, and rinsing with water. Subsequently, the metallized plasmonic transducer is integrated into a microfluidic chamber, which is manufactured by lamination of polymer layers using an origami-based self-alignment method [25]. A microfluidic chamber is structured in a double-side adhesive polymer layer (ARseal 8939, Adhesive Research, Ireland), which is designed using AutoCAD design software and cut with a cutting plotter (Silhouette portrait 2, Silhouette, Spain). The microfluidic chamber is sealed with a transparent polymethylmethacrylate layer (ME303016, Goodfellow, Spain) containing the inlet and outlet ports that are connected to mini-luer connectors and tubings (Microfluidic Chipshop, Germany). The connectors are integrated using ARseal 8939 O-rings of the same internal and external diameters. Figure S6 describes the manufacturing process used for the integration of the SPR transducer. To facilitate sample injection, fluid control and operation, a programable syringe pump is installed together with the optomechanical SPR system, as shown in Figure S7.

Beam shaping calculations

Figure 2 illustrates a representation of the beam propagation through various optical elements, such that the beam shows minimum angular dispersion at the metal-dielectric interface. The beam propagates from a virtual beam waist inside the laser, determined by

beam profiling, until the metal layer in which the plasmons are produced. Along this optical path, the beam experiences six propagations d_i in free space or in a medium of constant refractive index and is transformed at five curved, flat and tilted refractive interfaces.
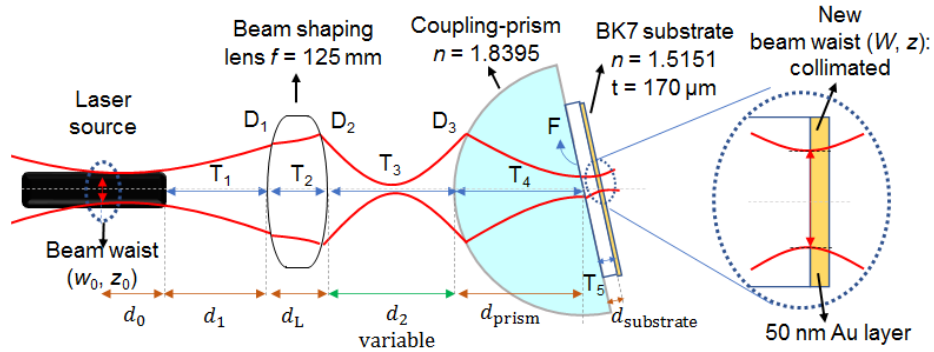

Figure 2: Schematic representation of Gaussian beam propagation along each refractive interface of the optical system.

The propagation of the Gaussian beam through the whole optical setup is done analytically by ray tracing analysis. The system is designed such that the final Gaussian at the metal surface fulfills

$$\frac{dW(z)}{dz} = 0 \qquad\qquad (3)$$

for least angular dispersion as shown in Figure 2, with $W(z)$ from Eq. (2), and it is resolved by transforming the complex q parameter from Eq. (1) (for further information about Gaussian beam propagation calculations see the supporting information).

An optical and illumination design software (OpticStudio™ 16.5, Zemax, UK) is used to design the optical system described in Figure 2. The optimization is done to find the

minimum value of the *GBPP* merit of function (*Gaussian beam paraxial position*), which resolves the system by placing the beam waist at the interface between the glass and the Au layer, with the distance d_2 as varying parameter. For optimized beam shaping it is indispensable to precisely characterize the original Gaussian laser beam. The half waist and its position, w_0 and d_0, are obtained by a highly precise beam profiling and fitting the data to the Gaussian beam intensity curve described in Eq. (2) (for further information about beam profiling see the supporting information).

Beam shaping experimental verification

The customized SPR system is built according to analytical and simulation results that lead to an optimized design. The verification of the system is done by several SPR measurements at varying distance d_2 with air as sample behind the Au layer. A motorized translational stage moves the semi-cylindrical prism along the optical axis to change the distance d_2. For the optimization, a variety of parameters of the SPR curve are analyzed, as shown in Figure 3, such as the maximum extinction A, the steepest negative slope S_{min} before the resonance condition, the curvature κ at resonance and the half width of the curve $\Delta\theta_{SPR\text{-}Smin}$ between θ_{Smin} and θ_{SPR}, also called half width at slope minimum, HWSM.
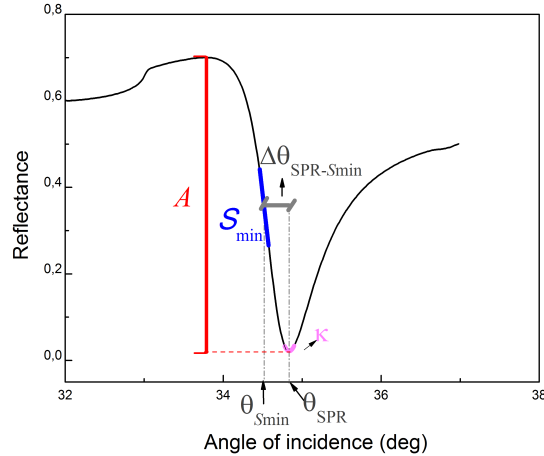
Figure 3: Characteristic parameters of a typical SPR curve in Kretschmann configuration [24]: Maximum extinction A, steepest slope S_{min}, angle at steepest slope θ_{Smin}, resonance angle θ_{SPR}, curvature at resonance κ, and angular distance between steepest slope and resonance $\Delta\theta_{SPR-Smin}$.

MATLAB (by MathWorks) is used for the analysis of the features, using precise local polynomial fits of the SPR curve around each parameter of interest to avoid noise artifacts and adverse smoothing effects.

Characterization of the optimized SPR system

Univariate analysis

Analytical figures of merit (AFOMs) such as sensitivity (SEN), analytical sensitivity (γ), *Root Mean Square Error of Cross Validation* (RMSECV), *Root Mean Square Error of Prediction* (RMSEP) and minimum detectable RI change or resolution (r_{Sensor}) are used to compare the performance of the optimized SPR system with beam shaping and the standard system without beam shaping. The systems are characterized by using UVA for each of the defined features of the SPR curves (A, S_{min}, θ_{Smin}, θ_{SPR}, κ and $\Delta\theta_{SPR-Smin}$) and calculating each figure of merit.

The calibration curves for the two SPR systems, with and without beam shaping, are built by measuring the SPR curves for five aqueous sucrose solutions, based on DI water, with different RI, due to increasing sucrose concentrations from 0% to 10%. The RIs of the sucrose solutions are measured using a commercial refractometer (Digital refractometer PCE-DRH1 series, PCE Instruments; Alicante, Spain), and RI values of 1.333, 1.3359, 1.3403, 1.3446 and 1.3475 are obtained for sucrose concentrations of 0%, 2%, 5%, 8% and 10%, respectively. The SPR curves are measured by angle interrogation between 46º - 53º with a sampling of 0.05º. Twenty measurements are carried out for each concentration and system design.

SEN of each SPR feature is calculated as the slope of the univariate calibration curve; RMSECV is estimated by Monte Carlo cross-validation, which performs 10 cycles with 70% of samples retained for calibration; RMSEP and resolution values for UVA are estimated using

$$RMSEP = \sqrt{\frac{\sum_{i=1}^{n}(P_i - O_i)^2}{n}}, \qquad (4)$$

$$r_{Sensor} = \frac{3 \cdot \sigma_{BLANK}}{SEN}, \qquad (5)$$

with P_i and O_i as the predicted and original value of the sucrose concentration and σ_{BLANK} as the standard noise deviation of several blanks.

Finally, the analytical sensitivity γ is defined as the ratio between sensitivity and instrumental noise σ_x, given by

$$\gamma = \frac{\mathrm{SEN}}{\sigma_x}.\qquad\qquad (6)$$

For simplicity, σ_x can be assessed from the residual matrix [26], as the difference between the predicted value P from the univariate calibration model and the original value O, where in this case P and O refer to the value of the RI. Similarly, in this particular case, γ is estimated as in [27].

Since the characteristic SPR features Y, which are A, S_{min}, θ_{Smin}, θ_{SPR}, κ and $\Delta\theta_{SPR\text{-}Smin}$, have different units and different magnitudes, relative changes of Y are analyzed by firstly centering each feature via subtraction of the average value and secondly dividing by the maximum value, $(Y_i\text{-}Y_{mean})/Y_{max}$, with Y_i as the value of the characteristic feature of an SPR curve at a sample concentration of i%.

Multivariate analysis

MVA is used to combine multiple features of the SPR curves, thereby gaining more information. By optimizing linear combinations of many characteristic features or variables, the performance in data analysis can be strongly improved compared to UVA. Among many existing multivariate analysis methods, partial least squares (PLS) is one of the most commonly used first-order calibration methods for the prediction of operational conditions (e.g. concentrations in chemometrics), which is a dimensionality reduction technique used for regression modeling [26]. Data is projected in a new subspace of latent variables which are linear combinations of original features from the SPR curves. Covariance between these new variables and RI conditions is maximized, such that the RMSECV and RMSEP are optimized. The multivariate calibration curves are built

similarly to the univariate method but using pseudo-univariate calibration curves based on the net analyte signal (NAS), which is defined as the part of the multivariate signal that the model relates to the predicted sample condition (e.g. RI or sucrose concentration). NAS is designated as **r*** and can be calculated as follows [28]:

$$\mathbf{r}^* = c\mathbf{b}/\|\mathbf{b}\|^2, \qquad (7)$$

where c indicates the predicted or observed values for the samples, and **b** is a vector containing the regression coefficients of the individual features, hence giving information about the relevance of individual variables. For inverse methods, such as PLS, a pseudo-univariate calibration model can be represented as reference analyte condition c_{ref} (e.g. original RI value) versus $\|\mathbf{r}^*\|$, with a least-squares fitted calibration curve

$$c_{\text{ref}} = b\|\mathbf{r}^*\|, \qquad (8)$$

where b is the slope, called the *inverse sensitivity* that represents $b = 1/\|\mathbf{s}^*\|$, with $\|\mathbf{s}^*\|$ as the sensitivity of the method. Accordingly, for the PLS model, SEN can be calculated as

$$\text{SEN} = \frac{1}{\|\mathbf{b}_{\text{PLS}}\|}, \qquad (9)$$

where $\|\mathbf{b}_{\text{PLS}}\|$ is the Euclidean norm of the PLS regression coefficients.

In the present case, the multivariate calibration model is built in MATLAB using Monte Carlo cross-validation, which performs 10 cycles with 70% of samples retained for calibration, and the optimum number of latent variables for prediction are calculated using the Haaland and Thomas criterion [29]. For each data set, the normalization to unity is done

using the mean normalization for each feature Y, which is $(Y_i - Y_{mean})/(Y_{max} - Y_{min})$, with Y_i the value at concentration i%, Y_{mean} the average value and Y_{max} and Y_{min} the maximum and minimum values of the specific feature. The SENs of the multivariate models for both systems, with and without beam shaping, are calculated from the pseudo-univariate calibration curves, as well as using Eq. (9). The RMSEP and the resolution values are calculated as for the univariate case.

RESULTS AND DISCUSSION

Simulations and analytical calculations for beam shaping

For the optimized SPR system a positive symmetric lens with a focal length of $f = 125$ mm is placed at $d_1 = 310$ mm, considering the dimensional restrictions for the assembly of the optomechanical system (Figure S7). The characteristics of the laser source are derived from beam profiling, with $w_0 = (0.27752 \pm 0.0009)$ mm and $d_0 = (-46.81 \pm 3.7)$ mm. The optimum design dimensions for both analytical and Zemax calculations is found at $d_2 = (178.07 \pm 0.38)$ mm, the error results from Gaussian error propagation considering the uncertainty from beam profiling of the original Gaussian laser beam. The final half beam waist of the Gaussian at the metal-dielectric interface is $W_f = (125 \pm 0.8)$ µm, with the corresponding Rayleigh range of $z_f = (77.56 \pm 0.96)$ mm, yielding stable operational conditions.

Experimental verification of optimized design

To verify the analytical and simulation results, four characteristic parameters of the SPR curve are analyzed: A, S_{min}, κ, and $\Delta\theta_{SPR-Smin}$ (see Figure 3). Figure 4 shows the variation

of these four characteristic parameters as a function of the distance d_2 between the beam shaping lens and the coupling-prism, showing clear extrema around the Rayleigh range. All measurements were conducted three times using air as dielectric medium. Table 1 gathers values for d_2 at which the individual parameters are optimized according to the position of the maximum or minimum (extremum) of each feature. The extrema indicate the position for strongest measurable SPR response and are empirically fitted by 2nd order polynomials. The feature S_{min} (steepest negative slope) shows a minimum for d_2 = 178.1 mm, which is in perfect agreement with the theoretical predictions. The other parameters show clear extrema as well, indicating an optimally shaped beam at the metal-dielectric interface, however, at slightly higher values of d_2. The corresponding d_2 values of all extrema are averaged and the error is calculated by Gaussian error propagation, obtaining d_2 = (182.5 ± 3.7) mm. These deviations can be explained by systematic measurement errors of geometrical distances in the setup, by interference effects impairing the resonance curve at high angles and the uncertainty of the fitted measurements. Considering all these errors, the experimentally optimized optomechanical configuration is in good agreement with the analytical and simulated calculations. Further measurements with liquid samples of varying RI were taken with the optimized SPR configuration, considering d_1 = 310 mm and d_2 = 182.5 mm as mentioned above.
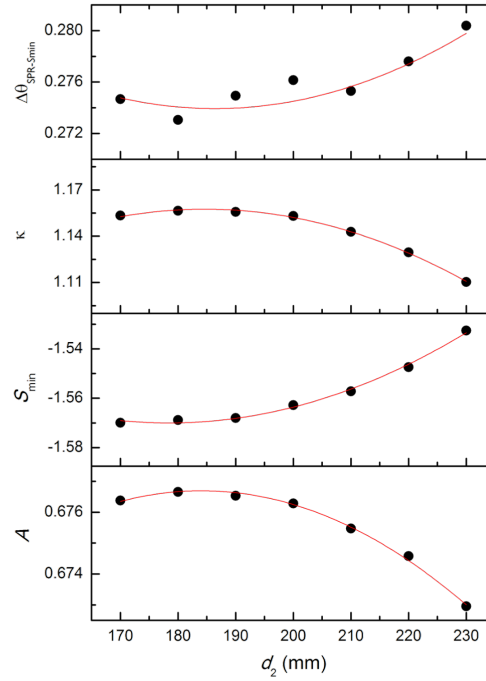
Figure 4: Experimental results for the design optimization of the SPR system by Gaussian beam shaping. SPR curves are measured three times using air as dielectric medium while varying the distance d_2 between the beam shaping lens and the prism (see Figure 2). The variations of the analyzed characteristic features A, S_{min}, κ and $\Delta\theta_{SPR\text{-}Smin}$ show clear extrema around the Rayleigh range.

Table 1: Experimental results for the SPR system design optimization by Gaussian beam shaping. Optimized d_2 values are calculated from the extrema of each feature, derived from the feature variation curves while varying d_2 (see Figure 4). The measurements are repeated three times for each feature and the error of the averaged d_2 values is calculated by Gaussian error propagation. Considering systematic errors of ± 3.7 mm for distance measuring through the whole optomechanical system, experimental and theoretical design results are in agreement.

New beam position	Experimental verification					Theoretical design
	A	**S_{min}**	**κ**	**$\Delta\theta_{SPR\text{-}Smin}$**	**Average**	
d_2 (mm)	183.8	178.1	184.0	184	182.5	178.07
Δd_2 (mm)	1.4	1.8	4.5	14	3.7	0.38

Characterization of the optimized SPR system

SPR measurements

The SPR system is tested, with and without beam shaping, in order to characterize the performance of both SPR configurations in measuring variations in RI, realized by changing concentrations of sucrose solution (see Figure 5). The SPR curves reflect stronger and sharper resonance for an optimally shaped incident Gaussian beam. Beam shaping leads to a higher maximum extinction A, hence steeper slope S_{min}, a narrower resonance reflected in the half width $\Delta\theta_{SPR-Smin}$ of the resonance curve, and a stronger curvature κ at resonance. For the resonance angle, the system without beam shaping shows slightly shifted resonance conditions with higher values for θ_{SPR} and θ_{Smin}, which can be explained by the asymmetric shape of the resonance dip and non-linear angular dispersion of the beam. However, angular shifts due to RI variations result in similar behavior for both systems, leading to higher SPR angles for increased RI of the dielectric medium. At higher RI, resonance curves become flatter, featuring decreased maximum extinctions A, and likewise weakened parameters S_{min}, κ, and $\Delta\theta_{SPR-Smin}$.

From these SPR curves, the calibration curves for UVA and MVA are generated for the characteristic features A, S_{min}, θ_{Smin}, θ_{SPR}, κ and $\Delta\theta_{SPR\text{-}Smin}$, which are calculated as input for the determination of several figures of merit (see supporting information for further details on univariate and multivariate calibration models).

Analytical figures of merit (AFOMs): univariate and multivariate analysis

The analysis of the SPR performance for both systems, with and without beam shaping, builds upon analytical figures of merit (AFOMs) such as the sensitivity (SEN), the analytical sensitivity (γ), the root mean square error of cross validation (RMSECV), the root mean square error of prediction (RMSEP) and the minimum detectable RI change (resolution). All these AFOMs calculated for the univariate and PLS multivariate calibration models as well as the statistical and prediction analysis for the PLS model for both systems, with and without beam shaping, are summarized in Table 2 and Table 3 and illustrated in Figure 6 and Figure 7.

Figure 6 shows the sensor sensitivity for the two system configurations, with and without beam shaping, when using UVA and MVA. SEN is defined as the ratio of the sensor signal variation to the change of RI. Figure 6a illustrates SEN values of six independent sensor signals obtained from UVA, measured as SPR curve features A, S_{min}, θ_{Smin}, θ_{SPR}, κ and $\Delta\theta_{SPR\text{-}Smin}$. The parameters that show the greatest relative change, in descending order, are the SPR curvature κ, the half-width $\Delta\theta_{SPR\text{-}Smin}$, the steepest slope S_{min}, and the

maximum extinction A, followed by the angular shifts (θ_{SPR} and θ_{Smin}) that show a noticeable lower relative change. The SEN values obtained from MVA, illustrated in Figure 6b, give evidence for strongly enhanced performance when the beam is shaped. The same trend is generally observed in UVA (see Table 2). MVA normally uses normalization procedures (e.g. mean normalization) to achieve dimensionless and scaled parameters and combines all the normalized signals such that the covariance with respect to RI is maximized. In the case of UVA, these normalizations cannot be used to evaluate and compare the relative changes of the features as independent sensor signals. Therefore, in UVA mean-max normalization is used to avoid the scaling of the sensing parameters to a fixed range (e.g. a commonly used range between 0 and 1) and thus represents the relative change of each parameter with respect to RI variations. In all cases the sensitivity SEN is given as a normalized quantity with respect to changes in refractive index (RIU: refractive index unit).
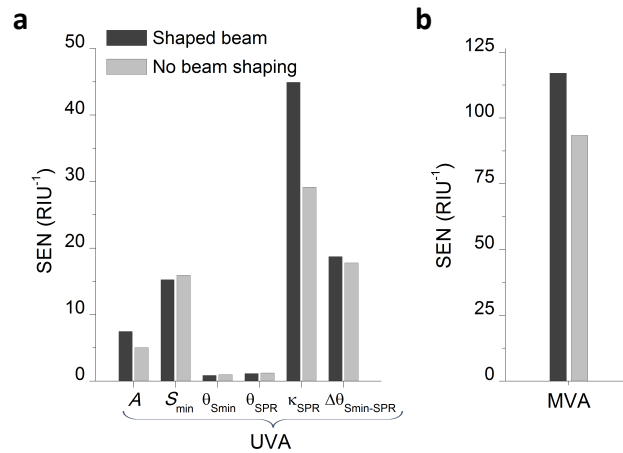

Figure 6: Sensitivity values for the SPR systems, with and without beam shaping, using UVA and MVA. (a) SEN values calculated from the normalized univariate calibration curves based on the characteristic features A, S_{min}, θ_{Smin}, θ_{SPR}, κ and $\Delta\theta_{SPR-Smin}$. SEN is calculated as the slope of the calibration curves of mean-max normalized data. (b) SEN values calculated from the multivariate PLS calibration model based on the mean normalized characteristic

When comparing the performance of different sensing signals, it is of utmost importance to use figures of merit that are independent of signal units and magnitudes. In this case, due to the different normalization procedures used for UVA and MVA methods, the parameters are scaled differently. Therefore, SEN cannot be used to compare the SPR performance of the single features, used as standalone sensing techniques in UVA, with the combined features, used as multiarray sensor in MVA. Nonetheless, it is possible to compare UVA against MVA using the analytical sensitivity (γ) as a better indicator for comparison purposes [26], as well as the root mean square error of prediction (RMSEP) and the minimum detectable RI change (resolution). The analytical sensitivity γ, which takes into account the sensitivity and the uncertainty of the data, again shows strong improvement using MVA. 15- and 4-fold enhancement is achieved when the best performance parameter of UVA is considered for the systems with and without beam shaping, respectively (see Figure 7.a, Table 2 and Table 3). The RMSEP values obtained from UVA indicate that the features with highest SEN are at the same time the parameters that lead to the greatest errors in prediction (see Figure 7.b and Table 2). For instance, for the optimized SPR system with beam shaping, S_{min}, κ and $\Delta\theta_{SPR\text{-}Smin}$ lead to especially high prediction errors, whereas A, θ_{Smin} and θ_{SPR} deliver much lower errors. For assessing performance, it is necessary to find a trade-off between SEN and RMSEP for choosing the best sensing parameters in UVA, such that high precision and high accuracy are achieved. This compromise can be guaranteed by γ as figure of merit. In general, higher γ values correspond to more sensitive and accurate sensing parameters with high SEN and low

RMSEP. For the optimized SPR system with beam shaping, the features with the highest analytical sensitivity are, in decreasing order, θ_{Smin}, θ_{SPR} and A, with considerable higher γ values, followed by κ, S_{min} and $\Delta\theta_{SPR\text{-}Smin}$.
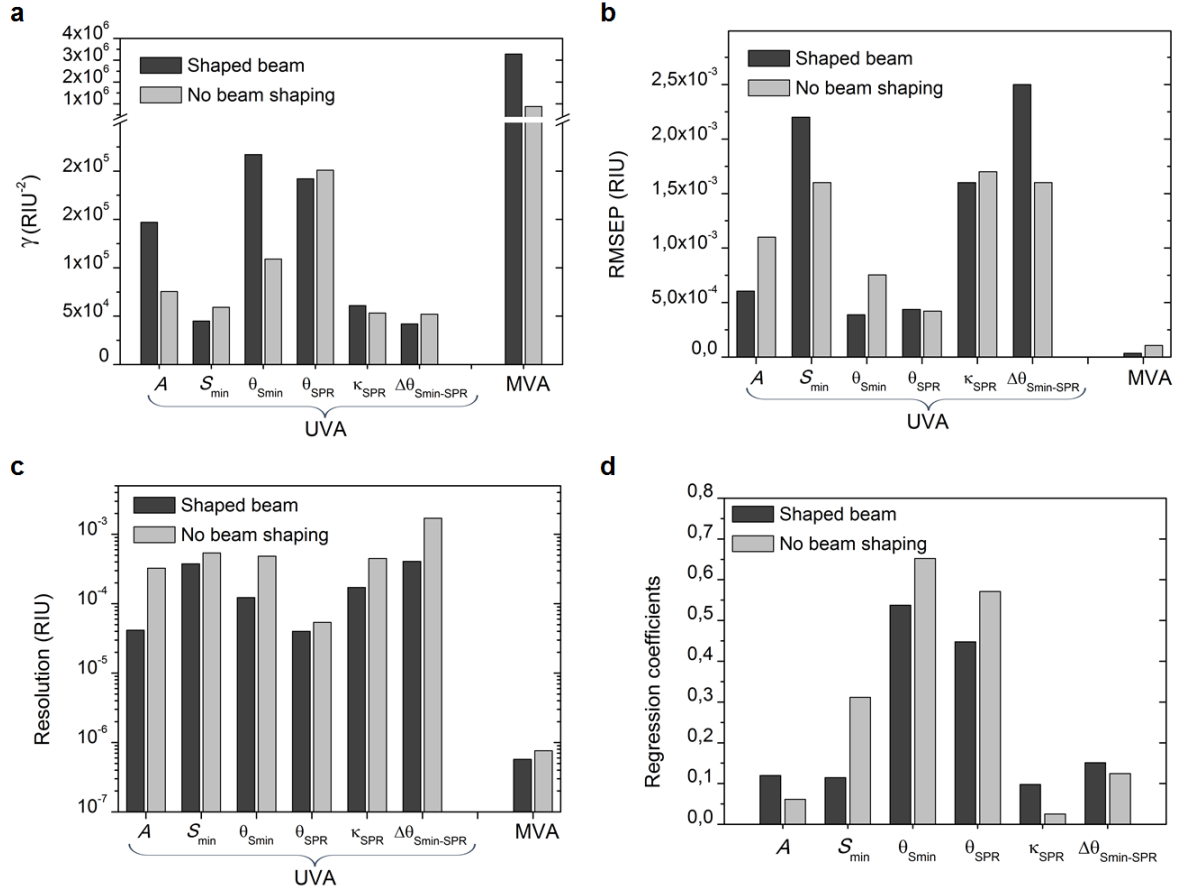

Figure 7: Figures of merit obtained from UVA and MVA calibration models for the SPR systems with and without beam shaping. UVA is based on different prediction parameters as characteristic features (A, S_{min}, θ_{Smin}, θ_{SPR}, κ and $\Delta\theta_{SPR\text{-}Smin}$), while MVA combines the information of all parameters for better prediction. (a) Analytical Sensitivity, γ. (b) RMSEP. (c) Resolution. (d) Normalized regression coefficients estimated by PLS. The coefficients shown are absolute values (some of the parameters are negative), original values of the regression coefficients are depicted in Figure S4.

The regression coefficients for MVA are shown in Figure 7d and Figure S4, which represent the contribution (or relevance) of each feature in PLS multivariate calibration model. As expected, a similar result as for γ is observed for the contributions of each parameter in the PLS multivariate calibration model. For the optimized SPR system with beam shaping, the regression coefficients show highest weight factors for θ_{Smin} and θ_{SPR}, followed by $\Delta\theta_{SPR-Smin}$, A, S_{min}, and κ, which demonstrates good agreement between γ and regression coefficients. Consequently, it is demonstrated that γ represents a suitable alternative AFOM to estimate the best performing parameters in UVA, as previously stated by Silva *et al.* [27], while MVA allows a deeper analysis by simultaneously considering various independent variables. Regression coefficients identify the relevance of each parameter in the multivariate model, by unveiling existing correlations between RI conditions and the variability of different SPR parameters.

Finally, resolution values obtained from UVA show the best performance for θ_{SPR} and A, as shown in Figure 7c. Furthermore, the resolution enhancement due to the Gaussian beam shaping is around 35% for the θ_{SPR} parameter (see Table 2). When comparing the developed systems with other systems found in literature, most of the reported detection resolutions for the SPR systems in angular interrogation are based solely on the resonance angle, and not using multiple parameters [30]. Additionally, it is highly important to make sure that the figures of merit are similarly defined. Sensor sensitivity can be expressed in different units depending on the measured signal or parameter (angle, wavelength, intensity, phase shift or other SPR-related parameters); moreover, different definitions for resolution can be found, even when the sensor resolution is always measured with the same unit, which is in this case RIU. For example, according to the

definition by Chung *et al.* [31], our two SPR systems, with and without beam shaping, present a resolution very similar to some home-made SPR systems [32-34] or the portable CORgi IIF SPR instrument from Plasmetrix. However, the definition by Chung *et al.* does not consider the standard noise deviation, thus not allowing for comparison of sensitivities and resolutions with commercial systems. Considering Eq. (5), our optimized system shows a resolution of 5.75×10^{-7} RIU, which demonstrates high performance and enhanced resolution due to Gaussian beam shaping and multivariate data analysis. Therefore, it offers higher resolution ranges than most portable SPR sensors and commercial SPR systems that are based on angular interrogation [30, 35, 36].

Table 2: Analytical figures of merit (AFOMs) estimated for both SPR systems, with and without beam shaping, and obtained from UVA calibration model. The measured sensor signals for building the AFOMs are the characteristic features A, S_{min}, θ_{Smin}, θ_{SPR}, κ and $\Delta\theta_{SPR-Smin}$, obtained from the SPR curves.

SPR system configuration	Evaluation parameters	AFOMs					
		SEN (RIU^{-1})		RMSECV (RIU)	RMSEP (RIU)	r_{Sensor} (RIU)	γ (RIU^{-2})
		mean-max norm	mean norm				
Optimized system: **Shaped beam**	A	7.46	89.25	6.08E-04	6.05E-04	4.17E-05	1.47E+05
	S_{min}	15.26	98.85	2.10E-03	2.20E-03	3.75E-04	4.49E+04
	θ_{Smin}	0.88	84.12	4.13E-04	3.88E-04	1.23E-04	2.17E+05
	θ_{SPR}	1.15	83.85	4.26E-04	4.37E-04	4.00E-05	1.92E+05
	κ	44.92	97.51	1.60E-03	1.60E-03	1.72E-04	6.09E+04
	$\Delta\theta_{SPR-Smin}$	18.74	104.7	2.40E-03	2.50E-03	4.07E-04	4.19E+04
Standard system: **No beam shaping**	A	5.05	83.13	1.10E-03	1.10E-03	3.25E-04	7.56E+04
	S_{min}	15.93	94.50	1.70E-03	1.60E-03	5.39E-04	5.91E+04
	θ_{Smin}	0.97	81.95	6.95E-04	7.54E-04	4.85E-04	1.09E+05
	θ_{SPR}	1.23	84.77	4.12E-04	4.22E-04	5.38E-05	2.01E+05
	κ	29.17	90.48	1.70E-03	1.70E-03	4.48E-04	5.32E+04
	$\Delta\theta_{SPR-Smin}$	17.78	83.35	1.40E-03	1.60E-03	1.70E-03	5.21E+04

Table 3: Summary of the statistical cross-validated calibration results, AFOMs and regression coefficients for both SPR systems, with and without beam shaping, obtained from a multivariate PLS inverse calibration model. The sensor signal used for AFOMs generation is the combination of mean normalized characteristic features A, S_{min}, θ_{Smin}, θ_{SPR}, κ and $\Delta\theta_{SPR-Smin}$, obtained from the SPR curves.

Calibration results	SPR system configuration	
	Shaped beam	No beam shaping
RMSECV (RIU)	3.81E-05	8.35E-05
Optimum nº of Latent Vectors	4	5
AFOMs		
SEN (RIU^{-1})	117.04	93.52
RMSEP (RIU)	3.57E-05	1.06E-04
r_{Sensor} (RIU)	5.75E-07	7.61E-07
γ (RIU^{-2})	3.28E+06	8.80E+05
Regression coefficients		
A	-0.0014	-0.0007
S_{min}	-0.0013	-0.0036
θ_{Smin}	0.0062	0.0075
θ_{SPR}	0.0052	0.0066
κ	0.0011	0.0003
$\Delta\theta_{SPR-Smin}$	0.0017	0.0014

CONCLUSIONS

Our results satisfactorily demonstrate that the optimization of the Gaussian beam propagation, such that the beam is shaped and aligned with least angular dispersion at the metal-dielectric interface, results in a sharper plasmonic resonance. As a result, three of the analyzed parameters from the SPR curve used as performance indicator features,

In addition, the combination of multiple features of the SPR curve using PLS enables a more precise analysis of the characteristic performance under different sample

conditions, resulting in an enhancement of the method. Therefore, combining the beam shaping with multivariate analysis we improve the performance of the SPR system, showing enhanced performance of three analytical figures of merit: analytical sensitivity, prediction error and resolution. Thereby, achieving enhanced resolution to the order of 5×10^{-7} RIU in angular interrogation, we overcome current limitations for biodetection in plasmonic detection systems.

ACKNOWLEDGEMENTS

CONFLICT OF INTERESTS

The authors declare that they have no conflict of interests.

SUPPLEMENTARY INFORMATION

Supplementary information includes (1) Beam profiling, (2) Gaussian beam propagation and (3) Supporting figures.

REFERENCES

1.   Oh, S.-H.; Altug, H., Performance metrics and enabling technologies for nanoplasmonic biosensors. *Nat. Commun.* **2018,** *9* (5263).

2.   Brolo, A. G., Plasmonics for future biosensors. *Nat. Photonics* **2012,** *6*, 709-713.

3.   Homola, J.; Koudela, I.; Yee, S. S., Surface plasmon resonance sensors based on diffraction gratings and prism couplers: sensitivity comparison. *Sens. Actuators B Chem.* **1999,** *54* (1), 16-24.

4.   de Mol, N. J.; Fischer, M. J., Surface plasmon resonance: a general introduction. *Methods Mol. Biol.* **2010**, 1-14.

5.   Patskovsky, S.; Kabashin, A. V.; Meunier, M., Near-infrared surface plasmon resonance sensing on a Si platform with nanoparticle-based signal enhancement. *Opt. Mater.* **2005,** *27* (5), 1093-1096.

6.   Kari, O. K.; Rojalin, T.; Salmaso, S.; Barattin, M.; Jarva, H.; Meri, S.; Ylipertuta, M.; Viitala, T.; Urti, A., Multi-parametric surface plasmon resonance platform for studying liposome-serum interactions and protein corona formation. *Drug Deliv. Transl. Re.* **2017,** *7*, 228-240.

7.   Jiang, L.; Yin, T.; Dubrovkin, A. M.; Dong, Z.; Chen, Y.; Chen, W.; Yang, J. K. W.; Shen, Z., In-plane coherent control of plasmon resonances for plasmonic switching and encoding. *Light Sci. Appl.* **2019,** *8* (1), 21.

8.   Yesilkoy, F.; Terborg, R. A.; Pello, J.; Belushkin, A. A.; Jahani, Y.; Pruneri, V.; Altug, H., Phase-sensitive plasmonic biosensor using a portable and large field-of-view interferometric microarray imager. *Light Sci. Appl.* **2018,** *7* (17152), 1-9.

9.   Dahlin, A. B.; Wittenberg, N. J.; Höök, F.; Oh, S.-H., Promises and challenges of nanoplasmonic devices for refractometric biosensing. *Nanophotonics* **2013,** *2* (2), 83-101.

10.   Cetin, A. E.; Coskun, A. F.; Galarreta, B. C.; Huang, M.; Herman, D.; Ozcan, A.; Altug, H., Handheld high-throughput plasmonic biosensor using computational on-chip imaging. *Light Sci. Appl.* **2014,** *3* (e122), 1-10.

11.   Coskun, A. F.; Cetin, A. E.; Galarreta, B. C.; Alvarez, D. A.; Altug, H.; Ozcan, A., Lensfree optofluidic plasmonic sensor for real-time and label-free monitoring of molecular binding events over a wide field-of-view. *Sci. Rep.* **2015,** *4* (6789), 1-7.

12.   Wang, W.; Mai, Z.; Chen, Y.; Wang, J.; Li, L.; Su, Q.; Li, X.; Hong, X., A label-free fiber optic SPR biosensor for specific detection of C-reactive protein. *Sci. Rep.* **2017,** *7* (16904), 1-8.

13.   Kaushik, S.; Tiwari, U. K.; Deep, A.; Sinha, R., Two-dimensional transition metal dichalcogenides assisted biofunctionalized optical fiber SPR biosensor for efficient and rapid detection of bovine serum albumin. *Sci. Rep.* **2019,** *9* (6987), 1-11.

14.   Xu, S.; Zhan, J.; Man, B.; Jiang, S.; Yue, W.; Gao, S.; Guo, C.; Liu, H.; Li, Z.; Wang, J.; Zhou, Y., Real-time reliable determination of binding kinetics of DNA hybridization using a multi-channel graphene biosensor. *Nat. Commun.* **2017,** *8* (14902), 1-10.

15.   Xue, T.; Liang, W.; Li, Y.; Sun, Y.; Xiang, Y.; Zhang, Y.; Dai, Z.; Duo, Y.; Wu, L.; Qi, K.; Shivananju, B. N.; Zhang, L.; Cui, X.; Zhang, H.; Bao, Q., Ultrasensitive detection of miRNA with an antimonene-based surface plasmon resonance sensor. *Nat. Commun.* **2019,** *10* (28), 1-9.

16.   Wu, F.; Thomas, P. A.; Kravets, V. G.; Arola, H. O.; Soikkeli, M.; Iljin, K.; Kim, M.; Shin, H. S.; Andreeva, D. V.; Neumann, C.; Küllmer, M.; Turchanin, A.; De Fazio, D.; Balci, O.; Babenko, V.; Luo, B.; Goykhman, I.; Hofmann, S.; Ferrari, A. C.; Novoselov, K. S.; Grigorenko, A. N., Layered material platform for surface plasmon resonance biosensing. *Sci. Rep.* **2019,** *9* (20286), 1-10.

17.   Anous, N. H.; Khalil, D., Performance evaluation of a metal-insulator-metal surface plasmon resonance optical gas sensor under the effect of Gaussian beams. *Appl. Opt.* **2014,** *53* (11), 2515-2522.

18.   Homola, J.; Yee, S. S.; Gauglitz, G., Surface plasmon resonance sensors: review. *Sens. Actuators B Chem.* **1999,** *54*, 3-15.

19.   Watad, I.; Abdulhalim, I., Spectropolarimetric Surface Plasmon Resonance Sensor and the Selection of the Best Polarimetric Function. *IEEE J. Sel. Top. Quantum Electron.* **2017,** *23* (2), 89-97.

20.   Anous, N.; Khalil, D.; Safwat, A. M. E., The effect of the Gaussian beam spot size on the performance of an SPR IR optical CO_2 sensor. *7th International symposium on High-capacity Optical Networks and Enabling Technologies (HONET)* **2010**, 19-21.

21.   Fries, F.; Fröbel, M.; Ang, P. Y.; Lenk, S.; Reineke, S., Real-time beam shaping without additional optical elements. *Light Sci. Appl.* **2018,** *7* (18), 1-11.

22.   Keigo, I., *Elements of photonics*. USA, 2002; Vol. 2.

23.   Kogelnik, H.; Li, T., Laser beams and resonators. *Appl. Opt.* **1966,** *5* (10), 1550-1567.

24.   Etxebarria-Elezgarai, J.; Rodríguez, C.; Echave, M.; Lopez, E.; Olaetxea, I.; Morant-Miñana, M. C.; Seifert, A. In *Improved plasmonic resonance by Gaussian beam shaping*, *2019 International Conference on Optical MEMS and Nanophotonics (OMN)*, Daejeon, Korea (South), IEEE: Daejeon, Korea (South), 2019; pp 208-209.

25.   Saez, J.; Basabe-Desmonts, L.; Benito-Lopez, F., Low cost origami fabrication of 3D self-aligned hybrid microfluidic structure. *Microfluid. Nanofluid.* **2016,** *116*, 1-7.

26.   Parastar, H.; Kirsanov, D., Analytical figures of merit for multisensor arrays. *ACS Sens.* **2020,** *5* (2), 580-587.

27.   Silva, M. A. M.; Ferreira, M. H.; Braga, J. W. B.; Sena, M. M., Development and analytical validation of a multivariate calibration method for determination of amoxicilin in suspension formulations by near infrared spectroscopy. *Talanta* **2012,** *89*, 342-351.

28.   Ferré, J.; Faber, N. M., Net analyte signal calculation for multivariate calibration. *Chemom. Intell. Lab. Syst.* **2003,** *69*, 123-136.

29.   Haaland, D. M.; Thomas, E. V., Partial Least-Squares Methods for spectral analyses. Relation to other quantitative calibration methods and the extraction of qualitative information. *Anal. Chem.* **1988,** *60*, 1193-1202.

30.   Ho, A. H.-P.; Wu, S.-Y.; Kong, S.-K.; Zeng, S.; Yong, K.-T., SPR Biosensors. In *Handbook of Photonics for Biomedical Engineering*, Ho, H. P. A.; Kim, D.; Somekh, G. M., Eds. Springer Science: 2017; pp 123-145.

31.   Chung, K.; Lee, J. S.; Kim, E.; Lee, K.-E.; Kim, K.; Lee, J.; D., K.; Kim, S. O.; Jeon, S.; Park, H.; Kim, D.-W.; Kim, D.-H., Enhancing the Performance of Surface Plasmon Resonance Biosensor via

Modulation of Electron Density at the Graphene-Gold Interface. *Adv. Mater. Interfaces* **2018,** (1800433), 1-8.

32.   Tang, Y.; Zeng, X.; Liang, J., Surface Plasmon Resonance: An introduction to a Surface Spectroscopy Technique. *J. Chem. Educ.* **2010,** *87* (7), 742-746.

33.   Zhang, C.; Chen, C.-J.; Settu, K.; Liu, J.-T., Angle-scanning surface plasmon resonance system with 3D printed components for biorecognition investigation. *Adv. Condens. Matter Phys.* **2018,** *5654010*, 1-7.

34.   Zhang, X.-L.; Liu, Y.; Fan, T.; Hu, N.; Yang, Z.; Chen, X.; Wang, Z.-Y.; Yang, J., Design and performance of a portable and multichannel SPR device. *Sensors* **2017,** *17* (6), 1435 (1-7).

35.   Preechaburana, P.; Gonzalez, M. C.; Suska, A.; Filippini, D., Surface plasmon resonance chemical sensing on cell phones. *Angew. Chem. Int. Ed. Engl.* **2012,** *51*, 11585-11588.

36.   Feltis, B. N.; Sexton, B. A.; Glenn, F. L.; Best, M. J.; Wilkins, M.; Davis, T. J., A hand-held surface plasmon resonance biosensor for the detection of ricin and other biological agents. *Biosens. Bioelectron.* **2008,** *23* (7), 1131-1136.